The Improved Comparative Reactivity Method (ICRM): measurements of OH reactivity at high-NOx conditions in ambient air

Wenjie Wang[1,3#], Jipeng Qi[1,2#], Jun Zhou[1,2], Bin Yuan[1,2*], Yuwen Peng[1,2], Sihang Wang[1,2], Suxia Yang[1,2], Jonathan Williams[4], Vinayak Sinha[5], Min Shao[1,2]

[1]Institute for Environmental and Climate Research, Jinan University, Guangzhou 511443, China.

[2]Guangdong-Hongkong-Macau Joint Laboratory of Collaborative Innovation for Environmental Quality, Guangzhou 511443, China.

[3]Multiphase Chemistry Department, Max Planck Institute for Chemistry, Mainz 55128, Germany.

[4]Atmospheric Chemistry Department, Max Planck Institute for Chemistry, Mainz 55128, Germany.

[5]Department of Earth and Environmental Sciences, Indian Institute of Science Education and Research (IISER), Mohali 140306, India.

#W.J.W. and J.P.Q. contributed equally to this work.

*Correspondence to: byuan@jnu.edu.cn

Abstract

The comparative reactivity method (CRM) has been developed more than a decade to measure OH reactivity (i.e. OH loss frequency) in both laboratory and field studies. However, accurate OH reactivity quantification remains challenging under real ambient condition, especially for OH reactivity measurements in high-NO_X (e.g. >10 ppbv) environments, as ambient NO enhance regeneration of OH radicals in the CRM reactor. To resolve this problem, we design a new improved CRM reactor (ICRM) and add NO into the system continuously, so that the HO_2 radical concentration is suppressed. We confirmed the appropriate level of NO by determining the maximum decrease in the pyrrole level caused by regenerated OH radicals from $NO + HO_2$. VOC-induced RO_2 radicals in the ICRM reactor were also found to react with NO, which lead to the re-generation of OH radicals thus the underestimation of OH reactivity. This effect was quantified by the calibration of representative VOC species at different NO levels, and the correction coefficients obtained were used to correct the measured OH reactivity. All these efforts resulted in reducing the uncertainty of the NO-artifact correction by at least an order of magnitude compared to the original CRM system. Additionally, these technological improvements also considerably reduced the systematic errors from pyrrole photolysis that exists in the original system. A new operation mode was proposed for ICRM, which is able to avoid the interference resulting from OH radicals produced by photolysis of residual humidity and save time for ambient measurement. The ICRM system was employed in a field campaign to measure OH reactivity and performed well with ambient NO levels ranged from 0 to 50 ppbv, which were typically observed in urban and suburban atmosphere.

1 Introduction

The hydroxyl radical (OH) is the most important oxidant in the daytime troposphere. It initiates the chemically removal of primary gaseous pollutants and in turn produces a host of secondary pollutants (A. Hofzumahaus, 1991; Atkinson, 2000; Roger Atkinson, 2003). The OH reactivity is defined as the sum of all OH reactive trace gas concentrations multiplied by their respective reaction rate coefficients with OH, as shown in Eq. 1. The OH reactivity is a fundamental property of the atmosphere in that it defines the overall loss frequency of OH radicals and hence the lifetime of OH. As such it is a useful atmospheric parameter for evaluating the level of reactive pollutants and it is closely related to atmospheric oxidation capacity and formation of secondary pollutants including ozone and secondary aerosols (Sinha et al., 2012; Yang et al., 2016; Pfannerstill et al., 2019).

$$R_{OH} = k_{CO}[CO] + k_{NO}[NO] + k_{NO_2}[NO_2] + k_{SO_2}[SO_2] + k_{O_3}[O_3] + \sum_i^n k_{VOC_i}[VOC_i]$$

$$(1)$$

Equation 1 defines the OH reactivity where R_{OH} is the total OH reactivity, k_{CO}, k_{NO}, k_{NO_2}, k_{SO_2}, k_{O_3}, and k_{VOC_i} represent the reaction rate coefficients between OH radicals and CO, NO, NO_2, SO_2, O_3, and volatile organic compounds (VOCs) species i, respectively. [CO], [NO], [NO_2], [SO_2], [O_3], and [VOC_i] are the concentrations of CO, NO, NO_2, SO_2, O_3, and VOCs species i, respectively.

Currently, two general methods are used to measure OH reactivity: (1) direct measurements of OH decay rates by laser-induced fluorescence (LIF) technique; (2) measuring the relative change of a reference substance with and without ambient air present by the comparative reactivity method (CRM). The LIF based technology has been used to measure OH reactivity in a variety of different environments and has provided many new insights into the budget of OH reactivity (Kovacs et al., 2001; Kovacs et al., 2003; Sadanaga et al., 2004; Sadanaga et al., 2005; Ingham et al., 2009; Lou et al., 2010). However, the cost, complexity, and large size of LIF systems are deterrents to the widespread deployment for field measurements (Sinha et al., 2008).

74   Such detector systems need to be built and cannot be bought directly from a supplier.

75   The CRM method measures OH decay rate indirectly by using the relative reaction rate

76   of a reference substance (pyrrole) with self-generated OH radicals in the presence and

77   absence of ambient air. The reference substance can be measured by an online

78   instrument, such as proton transfer reaction mass spectrometry (PTR-MS) (Sinha et al.,

79   2008; Sinha et al., 2009; Kumar et al., 2014) or a gas chromatograph (Nolscher et al.,

80   2012a; Praplan et al., 2017a; Praplan et al., 2019b). The CRM technique has proven to

81   be a useful supplementary technique to measure the total OH reactivity in ambient air,

82   with a more economical and portable setup than the LIF-based systems. Based on inter-

83   comparison between various OH reactivity techniques in the SAPHIR chamber, the LIF

84   type-instruments are generally more sensitive and less noisy than CRM instruments

85   (Fuchs et al., 2017).

86   The CRM approach has been applied to numerous field campaigns in recent years

87   to measure OH reactivity (Dolgorouky et al., 2012; Nölscher et al., 2014; Michoud et

88   al., 2015; Kim et al., 2016; Zannoni et al., 2016; Praplan et al., 2017b; Yang et al., 2017a;

89   Zannoni et al., 2017; Kumar et al., 2018; Pfannerstill et al., 2018; Pfannerstill et al.,

90   2019; Praplan et al., 2019a). However, this method is not suitable for the environment

91   with high-level NO_X, due to the pen-ray mercury lamp used to generate OH radicals in

92   CRM system also generates approximately equivalent amounts of HO_2 radicals that

93   may react with sampled NO to produce additional OH radicals (Sinha et al., 2008; Yang

94   et al., 2017a), which cause an enhanced consumption of pyrrole in the CRM system and

95   result in an underestimation of OH reactivity in sampled ambient air when NO exceeds

96   certain levels (Sinha et al., 2008). This NO interference prevents the CRM method from

97   providing high-quality data in emission exhausts and urban areas with high NO levels.

98   As a result, applications of the CRM method have been generally restricted to high

99   reactivity/low NO_X environments, including forests (Sinha et al., 2010; Kim et al., 2011;

100   Nolscher et al., 2012b; Praplan et al., 2019b; Pfannerstill et al., 2020), moderately

101   polluted cities (NO < 10 ppb) (Sinha et al., 2008; Praplan et al., 2017b), pristine marine

102   environments (Sinha et al., 2012; Zannoni et al., 2015), emission sources (e.g. gasoline

evaporation) (Wu et al., 2015), branch cuvette studies (Nölscher et al., 2013), and chamber studies (Nölscher et al., 2014) with little or no NO$_X$ present. One solution to this issue is to deliberately remove NO, before the sampled air is introduced into the reactor. However, the present technology is not able to remove NO selectively without affecting other reactive species (i.e., VOCs). The effect of NO on measured OH reactivity can be quantified by NO-correction experiments and the resulting correction curve applied to adjust ambient measurements according to simultaneously measured NO levels (Hansen et al., 2015; Yang et al., 2017a). However, the uncertainty of measured OH reactivity due to NO correction increases with NO concentration (Hansen et al., 2015; Michoud et al., 2015). Hansen et al. (2015) reported that the total uncertainty increases by up to a factor of 3 at NO$_X$ mixing ratios higher than 40 ppbv. Therefore, it calls for an improvement of the traditional CRM reactor for accurately quantifying OH reactivity at high NO$_X$ conditions. In addition to the NO effect, photolysis of pyrrole and VOCs, and the humidity difference between zero air and ambient air also influence measured OH reactivity (Sinha et al., 2008; Hansen et al., 2015; Zannoni et al., 2015).

The main purpose of this study is to improve the original CRM system to make it suitable for using in high-NO$_X$ conditions. We modified the structure of the original CRM glass reactor and add a certain amount of NO into the system to remove the generated but unwanted HO$_2$ radicals. We further characterized the improved CRM (ICRM) system by quantitatively evaluating the effect of the reaction of sample VOC-induced RO$_2$ with NO on measured OH reactivity. Additionally, the interference of pyrrole photolysis was also systematically evaluated. Finally, the ICRM system was deployed to measure OH reactivity under high-NO$_X$ conditions (0-50 ppbv) during a field campaign in the Pearl River Delta region of China.

2 Experimental and Methodology

2.1 The original CRM reactor

The schematic of the original CRM reactor is shown in Fig. 1a. Gas-phase pyrrole

mixed with zero air or ambient air is introduced through arm C at a constant flow. Arm A consists of a pen-ray spectral mercury lamp (**Analytik Jean; 90-0012-01**), over which nitrogen (humidified or dry) is passed through arm B at a constant flow rate. When humidified nitrogen is flowing and the mercury lamp is turned on, H_2O is photolyzed into OH and H radicals by the mercury lamp at 254 nm. The total air flow in the reactor exits through arm F and the concentration of pyrrole is monitored with a PTR-MS. A detailed description of the original CRM method has been reported by Sinha et al. (2008).

Figure 1(b) shows the four work modes of the original CRM method (Sinha et al., 2009). In C0 mode, the mercury lamp is turned off and high-purity dry nitrogen is introduced into the reactor through arm B. Pyrrole is introduced into the reactor with dry zero air through arm C. In C1 mode, the mercury lamp is turned on while everything else remains the same as C0. Pyrrole concentration decreases during C1 mode due to its photolysis reaction. In C2 mode, nitrogen flow in C1 is changed to humidified nitrogen to generate OH radicals, and the pyrrole concentration decreases to C2. In the final step, ambient air is introduced to the reactor through arm C in C3 mode. Based on pseudo-first-order assumptions (i.e., [pyrrole] $\geq$ [OH]), total OH reactivity (R_{OH}) is calculated as Eq. 2:

$$R_{OH} = C1 \times k_{pyr+OH} \times \frac{C3-C2}{C1-C3} \qquad (2)$$

Where k_{pyr+OH} is the rate coefficient for the reaction of pyrrole with OH radicals (1.28×10^{-10} cm^3·molecule^{-1}·s^{-1} (Dillon et al., 2012)), and C1, C2, and C3 represent pyrrole concentrations at the corresponding steps described above, respectively.

In C2 and C3 mode, OH radicals are produced by the photolysis of water vapor at atmospheric pressure as shown in R1. The generated H radicals from R1 reacts with O_2 of zero air or ambient air to generate HO_2 radicals, as shown in R2. When NO is present in the sampled ambient air, it can recycle OH by reacting with HO_2 (R3).

$$H_2O \xrightarrow{254nm} OH + H \qquad \text{R1}$$

$$H + O_2 + M \rightarrow OH + H \qquad \text{R2}$$

$$NO + HO_2 \rightarrow OH + NO_2 \qquad \text{R3}$$
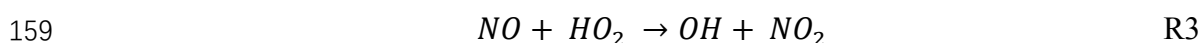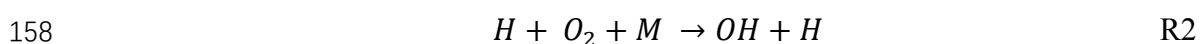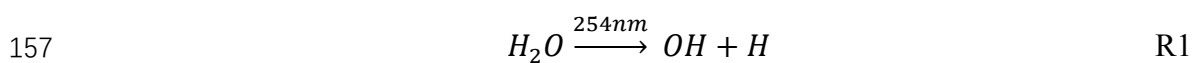
An underlying assumption of the CRM approach is that the influence of the species in ambient air on the production of OH radicals in the reactor is ignorable. The theoretical OH mixing ratio in the original CRM reactor is about 5 ~ 20 ppbv, which depends on the introduced pyrrole concentration to ensure the Pyrrole/OH ratio is 2:1~3:1. However, the additional OH radicals produced via R3 can react with pyrrole to cause an additional decrease in pyrrole relative to C2 mode, thus lead to the underestimation of OH reactivity.

2.2 The improved CRM reactor

In order to remove the interference of the reaction of HO_2 radicals with NO as discussed above, we modified the pipe structure of the original CRM reactor (Fig. 1c). We kept the length and volume of the glass reactor of the ICRM system similar to the original CRM system, but added a branch inlet G (1/4 inch OD glass; length 3 cm) in arm A to introduce steam of NO standard (Air Liquide; stated uncertainty 3%; 10.8 ppmv) mixed with zero air at a constant flow of 120 ml·min^{-1}. The typical flow rate inside the ICRM reactor is approximately 660 ml·min^{-1}. The flow rate of nitrogen (Air Liquide; 99.9995% purity) through arm B is 250 ml·min^{-1}. The input pyrrole (Linde Spectra Environment Gases; stated uncertainty 5%; 5.37 ppm) flow rate is 2.5 ml·min^{-1}. The total flow rate of pyrrole and zero air (Air Liquide; 99.9995% purity) through arm C is 290 ml·min^{-1}. With this modified structure of arm A, the HO_2 radicals, produced by the reaction of the generated H radicals near the mercury lamp and O_2 in introduced zero air, were converted to OH radicals by reacting with NO in the downstream of arm G. The interference induced by R3 can then be eliminated.

Arm A consists of one 1/2 inch OD (ID: 0.62 cm, length: 7 cm) glass tube and one 1/4 inch OD (ID: 0.32 cm, length: 5 cm) glass tube. The longer arm A is beneficial for longer reaction time of HO_2 with NO, but lower OH concentrations passing into the reactor due to wall loss. We chose an appropriate length of arm A (12 cm) to ensure appropriate OH concentration (4 ppbv) and reaction time of HO_2 with NO (~ 0.1 s). The purpose of the two-section structure is to ensure that the UV light is mostly confined within a 1/2 inch OD glass tube of arm A, as the diameter of arm A goes from

189 wide to slender. The new structure of arm A leads to lower OH concentrations

190 (decreased by approximately 50%) passing into reactor compared with the original

191 CRM system due to wall loss, but OH radicals produced from the reaction of HO_2

192 radicals with NO can partially compensate for this loss.

193 **2.3 The detection of pyrrole by PTR-MS**

194   The accuracy of pyrrole measurement is critical in determining OH reactivity for

195 CRM method. Here we used PTR-MS to detect pyrrole concentration. With a proton

196 affinity greater than water (Pyrrole: 209.2 $kcal \cdot mol^{-1}$; Water: 165.2 $kcal \cdot mol^{-1}$) (Sinha

197 et al., 2008), pyrrole is chemically ionized by proton transfer with H_3O^+ ions and the

198 product ions are detected using a quadrupole mass spectrometer. As highlighted by

199 Sinha et al. (2009), the sensitivity of PTR-MS instruments toward pyrrole is dependent

200 on humidity, and the pyrrole signal must be carefully calibrated for relative humidity

201 changes within the CRM reactor. The approach described by de Gouw and Warneke

202 (2007) was employed in this study to account for the effect of ion source and humidity

203 on the sensitivity of PTR-MS toward pyrrole (de Gouw et al., 2007). This approach

204 involves normalization of the pyrrole signal to a sum of reagent ion signals (H_3O^++X_R

205 $\times$ $H_3O^+ \cdot H_2O$) that leads to a normalized signal for pyrrole that is independent of

206 humidity. X_R, a scaling factor for the $H_3O^+ \cdot H_2O$ signal, is determined experimentally

207 by measuring the pyrrole signal from a standard mixture under different humidity

208 conditions. In this study, a relatively higher electric field parameter of the drift tube (i.e.

209 E/N) value of 153 Td was used to measure pyrrole, which can minimize the humidity

210 effect from water clusters in the PTR-MS instrument. As shown in SI, the best estimate

211 for X_R parameter was determined to be zero (Fig. S1), indicating negligible role for

212 $H_3O^+ \cdot H_2O$ in pyrrole detection by PTR-MS in this study.

213 **2.4 Other instruments of the ambient measurement campaign**

214   In order to test and validate the ICRM system for OH reactivity measurements

215 under high NO conditions, we conducted field measurements of OH reactivity at a

216 receptor site in the Pearl River Delta (PRD) region of China (Yang et al., 2017b; Tan et

al., 2019). Meanwhile, non-methane hydrocarbons (NMHCs) and oxygenated volatile organic compounds (OVOCs) were also measured by online gas chromatograph mass spectrometer and flame ionization detector (GC-MS/FID) (Wang et al., 2014a) and proton transfer reaction time-of-flight mass spectrometry (PTR-TOF-MS) (Yuan et al., 2017), respectively (Table S1). Inorganic trace gases, including CO, NO_2, NO, SO_2 and O_3, were measured by Thermofisher 48i CO analyzer, 2B Technologies Model 405nm NO_X analyzer, Thermofisher 42i NO_X analyzer, Thermofisher 43i SO_2 analyzer, and Thermofisher 49i O_3 analyzer, respectively. Detailed descriptions of these instruments can be found in previous studies (Wang et al., 2014b; Birks et al., 2018).

2.5. Zero dimensional box model

To test our understanding of the chemical processes occurring inside the ICRM reactor, results from laboratory experiments were compared with simulation from zero-dimensional (0-D) box model. The MCM v3.3.1 (Wolfe et al., 2016) was used as chemical mechanism in the box model. The use of the detailed mechanism aims at better representing the chemistry of peroxy radicals. In the box model, the initial concentrations of OH, HO_2, pyrrole, VOCs, CO, and NO were supplied, and the time-dependent variations of different compounds in the reactor are simulated. The initial concentrations of OH (4 ppbv), HO_2 (4 ppbv), and pyrrole (21 ppbv) are determined based on results from our experiments. The residence time in the reactor was about 11 s according to the volume of the reactor (120 cm^3) and the flow of introduced gases (660 ml·min^{-1}). An MCM subset was extracted for inorganic reactions, and reactions for propane, propene, and toluene. $C_3H_5O_2$ was used as a surrogate for the peroxy radicals from pyrrole, as the degradation of pyrrole is not included in MCM.

3 Results and discussion

3.1 Determination of the amount of NO addition

In addition to HO_2 produced from the reaction of H radicals with O_2, RO_2 produced from the reaction of pyrrole with OH also react with NO to recycle HO_2 and OH (R4-R6), and consume pyrrole. In order to eliminate the effect of HO_2 and RO_2 radicals, NO

supply with an appropriate concentration through arm G is needed. We optimized NO

concentration by testing the dependence of the change of the pyrrole concentrations on

the concentration of NO introduced through arm G (as described below and Fig. 2).

Figure 1d shows three work modes of the ICRM method. During the experiment, the

pyrrole concentration in the C1 mode (where N_2 and zero air were humidified and

mercury lamp is turned off) was 22 ppbv, which decreased to 18 ppbv when the mercury

lamp was turned on at 0 ppbv NO, implying that the generated OH radicals depleted ~

4 ppbv pyrrole. We varied the NO concentrations mixed with the zero air entering arm

G which resulted in NO concentrations in the reactor ranged from 0 to 150 ppbv, and

found out the appropriate NO level to consume all HO_2 and RO_2 produced in the glass

reactor. NO was mixed with zero air rather than nitrogen, as oxygen in zero air can

transform H radicals in arm A to HO_2 radicals. Pyrrole concentration decreases with the

increase of NO concentrations, reaching a minimum when NO concentration is circa

$40 \sim 50$ ppbv, and increased again when NO concentration exceeds 50 ppbv.

$$RH + OH + O_2 \rightarrow RO_2 + H_2O \qquad \text{R4}$$

$$RO_2 + NO + O_2 \rightarrow HO_2 + NO_2 + carbonyls \qquad \text{R5}$$

$$NO + HO_2 \rightarrow OH + NO_2 \qquad \text{R6}$$

$$RO_2 + HO_2 \rightarrow peroxide \qquad \text{R7}$$

$$NO + OH \rightarrow HONO \qquad \text{R8}$$
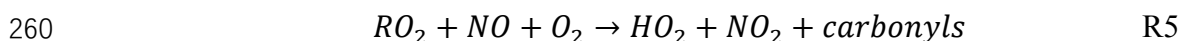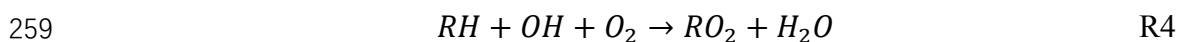
where RH represents pyrrole in the reactor or introduced ambient VOCs into the reactor.

The NO addition experiments are simulated in the box model. The simulated

pyrrole concentrations as a function of NO concentration is consistent with laboratory

experiments: with pyrrole concentrations decreasing at first and then increasing (Fig.

S2). When NO is not present in the reactor, the self-reactions of peroxy radicals

(HO_2+HO_2, HO_2+RO_2) dominate the sink of HO_2 and RO_2 (Fig. S3). As NO is

introduced into the reactor, the reaction of NO with HO_2 or RO_2 competes with the self-

reactions of peroxy radicals. With more NO introduced, the produced OH radicals from

the reaction of HO_2 with NO increase, leading to the decrease of pyrrole concentration

(Fig. S3). As the NO concentration exceeds 50 ppbv, pyrrole concentrations increase

274 again, due to large excess NO competes with pyrrole for reaction with OH radicals. The

275 remaining NO concentration outflowing from the reactor increases with the introduced

276 NO concentrations (Fig. S2), indicating that excessive NO is needed to compete with

277 the self-reactions of peroxy radicals. Based on laboratory measurement, the remaining

278 NO concentration outflowing from the reactor is ~18 ppbv when the introduced NO

279 concentration at 50 ppbv. The laboratory measurements and simulated results both

280 suggest that 40 ~ 50 ppbv is the lowest NO concentration needed to transform HO_2 and

281 RO_2 to OH to the largest extent. The higher introduced NO concentration had a

282 negligible effect on the increase in OH production from HO_2 and RO_2. Thus, we

283 introduce 50 ppbv NO concentration into the ICRM reactor in the experiments in this

284 study. Under this optimized condition, the pyrrole concentration decreased to 12.3 ppbv,

285 indicating the total OH radical concentration including production from UV lamp and

286 from the reaction of HO_2 with NO is about 10 ppbv in the ICRM system. The

287 concentration of pyrrole in this scenario is regarded as the C2 mode for ICRM system.

288 It worth noting that the determined NO concentration can vary slightly as OH

289 generation performance changes (e.g. humidity change in the region of the pen-ray

290 mercury lamp).

291 Under the determined optimal NO level through arm G, it is necessary to ensure

292 that the OH production from HO_2 and pyrrole-induced RO_2 will not manifest itself

293 when ambient NO is introduced through arm C. For this purpose, we compared

294 measured and true OH reactivity of NO by passing a series of NO concentrations (0 ~

295 700 ppbv) mixed with zero air through arm C into the reactor (Fig. 3). In this test, no

296 other reactive gases were introduced into the system except NO. Measured OH

297 reactivity of NO (k_{NO} = 9.7×10^{-12} cm^3 $molecule^{-1}$ s^{-1} according to IUPAC lasted

298 evaluation in November 2017) agreed well with the corresponding true values,

299 indicating that HO_2 radicals have been fully consumed, and pyrrole peroxy radicals

300 were effectively converted to carbonyls and nitrates by NO introduced through arm G.

301 **3.2 Calibration for OH reactivity of VOCs**

302 Several reactive VOC species were used to validate and calibrate the ICRM system,

303 including methane, propane, propene, toluene, and mixed gases including 16 VOC

304 species (acetaldehyde, methanol, ethanol, isoprene, acetone, acetonitrile, methyl vinyl

305 ketone, methyl ethyl ketone, benzene, toluene, o-xylene, α-pinene, 1,2,4-

306 trimethylbenzene, phenol, m-cresol, naphthalene). These VOC species were introduced

307 into the system through arm C at various reactivity (0 ~ 200 s^{-1}). Figure 4 (a) presents

308 the plots of the measured (R_{meas}, s^{-1}) versus true OH reactivity (R_{true}, s^{-1}) of these species.

309 R_{meas} is lower than R_{true} for almost all species with the slopes of linear fittings ranging

310 from 0.60 to 0.72. The slopes of methane, propane, propene, toluene, and mixed gases

311 are 0.60, 0.64, 0.64, 0.64, and 0.72, respectively. The OH reactivity calibration of SO$_2$

312 and CO indicates that the linear fitting slope of R_{meas} versus R_{true} is 0.35 and 0.40,

313 respectively (Fig. 4 b), which is lower than that of VOCs. It is worth mentioning that

314 the intercept of the line in Fig. 4 is not zero which indicates that at low OH reactivity

315 the ICRM methods lacks sensitivity.

316 Equation 2 is valid only under near pseudo-first-order conditions (i.e. when

317 [pyrrole] >> [OH]). In this study, the [pyrrole] to [OH] ratio is set at 2.5, which will

318 cause significant systematic errors. We plot the calculated reactivity, obtained by

319 applying Eq. 2 to the numerical simulations of the pyrrole concentration (C2 and C3)

320 at [Pyrrole]/[OH] = 2.5 after OH had reacted to zero, versus the true reactivity. The

321 correction curve indicates that the calculated reactivity underestimates the true

322 reactivity by about 5%. After considering this interference, the slope of calibration

323 shown in Fig. 4 (a) and 4 (b) decreased to 0.57 ~ 0.68 for VOCs, 0.38 for SO$_2$ and 0.33

324 for CO, respectively. Therefore, the deviation of pseudo-first-order conditions cannot

325 explain the calibrated slopes for VOCs, CO and SO$_2$ being lower than one.

326 The lower calibrated slopes for VOCs than one can be related to secondary

327 chemistry of VOC-generated RO$_2$ radicals with NO. When more VOCs are introduced

328 into the reactor, additional RO$_2$ radicals produced from the reaction of VOCs with OH

329 will react with excessive NO in the reactor thus increase the recycled OH (R4-R6). The

330 recycled OH from RO$_2$ will deplete pyrrole thus leading to a R_{meas} lower than the R_{true}.

331 We deduce that this is the reason for the linear fitting slopes in Fig. 4 lower than one.

332   For specific VOC species, the decrease in pyrrole concentration due to recycling OH

333   depends on the true OH reactivity of VOCs, NO concentrations and the efficiency of

334   organic nitrate production ($RO_2 + NO \rightarrow RONO_2$) in this system. The consistency in

335   the linear fitting slopes of different VOC species indicates that the RO_2 + NO reactions

336   for the investigated VOCs are similar. This is in agreement with the simulated results

337   (Fig. S4). Similarly, the produced HO_2 from the reactions of CO and SO_2 with OH will

338   end up recycling OH in the excess NO environments and thus reduce the fitting slopes.

339   The lower fitting slope of SO_2 and CO than that of VOCs is because SO_2 and CO react

340   with OH to produce HO_2, which has higher efficiency to produce OH by reacting with

341   NO than RO_2 that goes through two steps ($RO_2 \rightarrow HO_2$, and $HO_2 \rightarrow OH$). Here, we define

342   the linear fitting slopes in Fig. 4 as correction coefficients with regard to the calibration

343   for OH reactivity of VOC, CO and SO_2 (characterized by α_{VOC}, α_{CO} and α_{SO2}) at ambient

344   NO = 0 ppbv.

345   To further evaluate the performance of the ICRM system with elevated NO_X

346   concentrations in ambient air, a series of NO concentrations were introduced into the

347   reactor through arm C both with constant reactivity from different VOC species and

348   with different reactivities provided by the same species. Of all experimental conditions,

349   the R'_{meas} (The R'_{meas} is defined as the corrected R_{meas} by correction coefficient α_{VOC})

350   was observed to decrease with increased NO concentration, and thus the difference

351   between R_{true} and R'_{meas} ($R_{true} - R'_{meas}$) increases with increased NO concentrations for

352   the four VOC standard gases (Fig. 5a and b). This is because the reaction rate of RO_2

353   with NO increases with NO concentrations leading to enhancement of the recycled OH.

354   Similar to previous study (Michoud et al., 2015; Praplan et al., 2017b; Yang et al.,

355   2017a), the difference between R_{true} and R'_{meas} ($R_{true} - R'_{meas}$) increases with NO

356   concentrations for different VOC species and different reactivity levels. Besides, the

357   difference between R_{true} and R'_{meas} ($R_{true} - R'_{meas}$) also increases with NO concentrations

358   for CO and SO_2 with slope of 0.11 and 0.10 respectively (The R'_{meas} is defined as the

359   corrected R_{meas} by correction coefficient α_{CO} and α_{SO2}) (Fig. 5 c). However, the

360   difference of NO effects between VOCs and CO (and SO_2) as shown in Fig. 4 and Fig.

361   5 has not been reported in previous studies about CRM system.

362   Previous studies have reported that NO had a large effect on the difference between

363   R_{true} and R_{meas} in the CRM systems (Note that the R_{meas} is not corrected in previous

364   studies) (Hansen et al., 2015; Michoud et al., 2015; Yang et al., 2017b). This NO-effect

365   is not only due to the reaction of HO_2 with NO, but also due to the reaction of pyrrole-

366   produced and VOC-produced RO_2 with NO. Figure S5 compares the effect of NO on

367   (R_{true} - R_{meas}) in the original CRM system (reported by previous studies) with that in the

368   ICRM system (this study). Far larger NO effects were reported in the original CRM

369   system than in the ICRM system. For example, the presence of ambient NO at 50 ppbv

370   leads to R_{meas} lower than the R_{true} by $70 \sim 232$ s^{-1}, at least an order of magnitude higher

371   than the NO artifact in the ICRM system, which leads to R'_{meas} lower than the R_{true} by

372   8.8 s^{-1}. This is because both HO_2 and pyrrole-induced RO_2 are fully removed by the

373   introduced NO in advance in the ICRM system, thus the remaining influencing factor

374   is the reaction of ambient VOCs-induced RO_2 with NO. The uncertainty due to the NO-

375   artifact correction in the ICRM system was predicted to be far lower than that of the

376   original CRM system, as the absolute change of OH reactivity caused by NO is reduced

377   by removing HO_2 and pyrrole-induced RO_2. Despite the ICRM system not being able

378   to remove the NO effect entirely, it does lead to a significant decrease in the uncertainty

379   of the NO-artifact correction.

380   Due to the different behaviors of VOCs, SO_2 and CO at high NO conditions, in

381   order to get accurate OH reactivity, it is necessary to conduct NO-correction for VOCs,

382   SO_2, and CO individually. Note that this issue may also present in the original CRM

383   system, but it was ignored in previous studies. For the ICRM system, we use the

384   following formula to determine the true OH reactivity of VOCs:

385   $R_{meas} = R_{true\ NO+NO_2} + R_{true\ O_3} + \alpha_{CO}(R_{true\ co} - f_1[NO]) + \alpha_{SO_2}(R_{true\ SO_2} -$

386   $\qquad f_1[NO]) + \alpha_{VOC}(R_{true\ voc} - f_2)$ \hfill (3)

387   $R_{true\ VOC} = \frac{1}{\alpha_{VOC}}(R_{meas} - R_{true\ NO+NO_2} - R_{true\ O_3} + \alpha_{CO}f_1[NO] +$

388   $\qquad \alpha_{SO_2}f_1[NO] + \alpha_{VOC}f_2 - \alpha_{CO}R_{true\ co} - \alpha_{SO_2}R_{true\ SO_2})$ \hfill (4)

389   where R_{meas} is the measured OH reactivity by the ICRM system as defined above.

The $R_{\text{true VOC}}$ is the true OH reactivity of VOCs. $R_{i\text{ true}}$ was calculated from measured concentrations of species i (i=NO, NO₂, O₃, SO₂ and CO) multiplied by the rate coefficient of the reaction of species i with OH. The R_{meas} and R_{true} of NOx (=NO+NO₂) was close to 1:1 as shown in Fig. 3 and Fig. S6. α_{CO}, α_{SO_2}, and α_{VOC} are the correction coefficients with regard to the calibration for OH reactivity of CO, SO₂ and VOC at ambient NO = 0 ppbv, respectively. Note that the α_{VOC} is the mean slope of Fig. 4a. f_1 and f_2 are the correction coefficients which regard to the effect of ambient NO on ($R_{\text{true}} - R'_{\text{meas}}$). Note that the f_1 is the mean value Fig. 5c, and the f_2 is the fitting result both Fig. 5 a and b ($f_1 = 0.105$; f_2=0.20*[NO]-4.8*10⁻⁴*[NO]², as shown in Fig S5). After getting $R_{true\,VOC}$, the total OH reactivity (R_{tot}) was then calculated as the summation of $R_{true\,VOC}$, $R_{true\,NO+NO_2}$, $R_{true\,O_3}$, $R_{true\,SO_2}$, and $R_{true\,co}$:

$$R_{tot} = R_{true\,VOC} + R_{true\,NO} + R_{O_3} + R_{true\,NO2} + R_{true\,CO} + R_{true\,SO_2} \qquad (5)$$

In this study, we calibrated four individual representative VOC species (methane, propane, propene, toluene). In addition, we also calibrated the mixed standard gases with 16 VOC species including representative oxygenated VOCs (acetaldehyde, methanol, ethanol, acetone, acetonitrile, methyl vinyl ketone, methyl ethyl ketone), biogenic VOCs (isoprene, α-pinene), typical aromatics (benzene, toluene, o-xylene, 1,2,4-trimethylbenzene, naphthalene, phenol, m-cresol). The calibration slope is close to those of the four individual VOC species, indicating that the RO₂ + NO reactions for these investigated VOCs should be similar. Nevertheless, given that there are different VOCs compositions in different environment such as forest, urban area and emission sources, calibrations for more individual VOCs species might be also needed.

3.3 Additional potential interference related to NO addition

In order to assess the extent of any additional interferences due to NO addition, we further consider the following effects.

In arm A, the photolysis of O₂ introduced through arm G by the mercury lamp produces O₃. Besides, the NO introduced through arm G reacts with HO₂ to generate NO₂, which can also photolysis to generate NO and oxygen atoms, and subsequently

418   O_3. We monitored O_3 concentration through the arm F using an O_3 monitor. O_3

419   concentration flowing out of arm F was less than 5 ppbv, which has a negligible

420   influence on the pyrrole concentrations and the R_{meas}, considering the pyrrole+O_3

421   reaction rate constant $k_{O3+pyrrole} = 1.57 \times 10^{-17}$ cm^3 $molecule^{-1}$ s^{-1} (Atkinson et al., 1984)

422   is several orders of magnitude slower than the pyrrole + OH reaction rate constant

423   ($k_{pyrrole+OH} = 1.28 \times 10^{-10}$ cm^3 $molecule^{-1}$ s^{-1}). The ozone concentration was low, as excess

424   NO was introduced to the reactor and the remaining NO titrates O_3 back to NO_2.

425   In the C3 mode of the ICRM, sample ambient O_3 can react with the high-levels

426   NO in the reactor, which might interfere with R_{meas}. We characterize this interference

427   by introducing a series of O_3 concentrations into the reactor through arm C. As O_3

428   concentrations lower than 40 ppbv, O_3 has a negligible effect on OH reactivity (Fig. 6).

429   Interestingly, R_{meas} first increases and then decrease with increasing O_3 concentrations.

430   The reaction rate coefficient of OH with NO_2 is slightly higher than with NO, which

431   are 1.2×10^{-11} cm^3 $molecule^{-1} s^{-1}$ (Atkinson et al., 2004) and 9.7×10^{-12} cm^3 $molecule^{-1} s^{-1}$

432   at 298K, respectively. With the increase of introduced O_3 concentration, higher NO_2 is

433   produced, which causes an increase in R_{meas}. As NO is consumed completely by O_3,

434   excessive O_3 can further react with NO_2 to produce NO_3 radicals, which can deplete

435   pyrrole ($k = 1.80 \times 10^{-10}$ cm^3 $molecule^{-1}$ s^{-1}) (Cabanas et al., 2004) and lead to the

436   decrease in R_{meas}. Overall, OH reactivity exhibited little change (< 2 s^{-1}) with the

437   increase of O_3 concentrations ($0 \sim 160$ ppbv), indicating that the introduced O_3 plays a

438   negligible role in R_{meas}. This is another advantage of ICRM compared with the original

439   CRM, which needs an ozone correction as the reaction of O_3 with HO_2 gives OH back

440   (Fuchs et al., 2017).

441   According to model simulation, the produced NO_2 from the reaction of NO with

442   HO_2 increases with introduced NO concentrations (Fig. S2). The produced NO_2 can

443   deplete OH (OH + NO_2 $\rightarrow$ HNO_3) and thereby lead to an increase in the pyrrole

444   concentration. When introduced NO with a concentration of 50 ppbv, the produced NO_2

445   was 25 ppbv, corresponding to 6.2 s^{-1} OH reactivity (Fig. S2). However, this process

446   doesn't interfere with the R_{meas} as the produced NO_2 is the same in both C2 and C3

447   modes leading to this effect canceling out in the two modes.

448   Finally, the reaction time between HO_2 and NO should be noted. The initial HO_2

449   concentration is about 4 ppbv. The lifetime of HO_2 at 50 ppbv NO is at the time scale

450   of 0.1 s, given that the reaction rate constant of $NO+HO_2$ is 8.1×10^{-12} cm^3 $molecule^{-1}$

451   s^{-1} (Sander, 2006). The rection time of $NO+HO_2$ in arm A is estimated to be around ~

452   0.1 s, during which most of HO_2 will be consumed. Hence there will be only a small

453   fraction of HO_2 entering the main body of the reactor.

454   **3.4 Photolysis of pyrrole**

455   Photolysis of pyrrole in the CRM method introduces additional uncertainties and

456   complexity in the determination of OH reactivity (Sinha et al., 2008; Hansen et al.,

457   2015; Michoud et al., 2015; Zannoni et al., 2015). To investigate the effect of the ICRM

458   system on the interference from photolysis, we turn the mercury lamp off and on to test

459   the variation in pyrrole concentrations under dry conditions (no humidification).

460   Compared with the condition where the mercury lamp is turned off, pyrrole

461   concentrations decreased by < 3% after the mercury lamp was turned on (Fig. S7),

462   which caused R_{meas} increase of 0.55 s^{-1} when the R_{true} was 20 s^{-1}. This result indicates

463   that the photolysis of pyrrole is weak enough to be negligible in the ICRM system. This

464   smaller photolysis of pyrrole closely relates to the improved design of reactor structure.

465   Arm A consists of two section of glass tube with 1/2 inch OD and 1/4 inch OD,

466   respectively (Fig. 1c). UV light is mostly confined in 1/2 inch OD glass tube of arm A,

467   as the glass tube is constructed with decreasing diameter following the direction of gas

468   flow. This reduces the amount of UV light getting into the main reaction part of the

469   reactor. The improved structure of arm A leads to lower OH concentrations (decreased

470   by approximately 50%) passing into reactor due to wall loss, but the OH radicals

471   produced from the reaction of HO_2 radicals with NO can partially compensate for this

472   loss. In comparison, the pen-ray mercury lamp was very close to the main body of the

473   reactor in the original CRM reactor, to maximize the OH entering the reactor by

474   minimizing wall loss. However, this will lead to the photolysis of pyrrole, as high as

475   25% (Sinha et al., 2008; Hansen et al., 2015). The change of the structure of arm A also

476 ensures that the photolysis of H_2O, HONO, NO_2, and VOCs inside the ICRM reactor is

477 weaker than that in the original CRM system. In this system, OH reacts with introduced

478 NO or ambient NO to produce HONO, which can reproduce OH and NO by photolysis.

479 As we have improved the structure of arm A to avoid UV light entering main body of

480 the reactor, photolysis of HONO is expected to be low. In addition to our design change,

481 previous studies have reported that the photolysis of pyrrole can be also lowered to

482 below 5% by changing the UV mercury lamp position in the setup (Michoud et al.,

483 2015; Zannoni et al., 2015).

484   In the original CRM system, C1 instead of C0 is used as the initial amount of

485 pyrrole in order to avoid the interference of pyrrole photolysis. The C1 mode, where

486 dry N_2 and zero air are used meanwhile the mercury lamp is turned on, was measured

487 every 12 h for a duration of 2 h (Sinha et al., 2008; Hansen et al., 2015). The length of

488 the duration is necessary to reach the driest conditions possible to minimize residual

489 OH in the reactor. It should be noted that this procedure can result in an underestimation

490 of C1, as it is difficult to remove all trace amounts of water molecules from surfaces

491 and in nitrogen and zero air flowing through the reactor, which is able to produce extra

492 OH by photolysis (Hansen et al., 2015; Michoud et al., 2015; Zannoni et al., 2015). The

493 underestimation of C1 will result in an overestimation of OH reactivity. The

494 significantly smaller photolysis of pyrrole for the ICRM system allows us to measure

495 the C1 mode differently. Here, the condition that N_2 and zero air are humidified while

496 the mercury lamp is turned off is regarded as C1. The new C1 mode is able to avoid the

497 interference resulting from OH radicals produced by photolysis of residual humidity

498 since the mercury lamp is turned off and OH will not be produced. Besides, the C1

499 mode in ICRM is measured every 12 h for a duration of 15 min, which also saves time

500 compared with C1 mode in original CRM.

501 **3.5 Humidity difference between zero air and ambient air**

502   The variation of humidity between the C2 (wet zero air) and C3 (ambient air)

503 measurements could result in a change in OH production rate in the CRM reactor, which

504 in turn could lead to a C2 measurement not representative of the OH production rate

505 observed during the C3 measurement (Sinha et al., 2008; Dolgorouky et al., 2012).

506 Although the use of a catalytic converter or dynamic humidification of zero air can help

507 to reduce differences in humidity between C2 and C3 modes, small differences still

508 exist (Michoud et al., 2015). Besides, while catalytic converters can be used to generate

509 zero air with the same humidity as ambient air, these converters cannot remove NOx

510 species and thus are not suitable for OH reactivity measurements in urban and suburban

511 areas with high NOx conditions (Hansen et al., 2015).

512 To investigate the influence of humidity differences between C2 and C3 on the

513 R_{meas} in the ICRM system, we test the response of pyrrole concentration to humidity by

514 introducing zero air with different humidities through arm C at mode C2. The ratio of

515 $H_3O^+(H_2O)$ to H_3O^+ (m37/m19) is selected to represent the level of different humidity.

516 Figure 7 (a) presents the dependence of pyrrole concentrations on m37/m19 at mode

517 C2. Pyrrole concentrations slightly decrease with the increase in m37/m19. It must be

518 noted that this dependence is not due to the humidity dependence of the PTR-MS

519 sensitivity toward pyrrole, but the change in OH production in the reactor, as the

520 normalization procedure of pyrrole signal described in Sect. 2.3 was applied to all

521 pyrrole measurements. The maximum difference of m37/m19 between C2 mode and

522 C3 mode is about 0.01 corresponding to RH changing by ~ 30% (Fig. 7 b), which lead

523 to pyrrole changed by ~ 0.26 ppbv and thus the R_{meas} changed by ~1.9 s^{-1} when the R_{true}

524 is 20 s^{-1}. This result indicates that the influence of humidity change on OH

525 concentrations and subsequently R_{meas} cannot be ignored even though the structure of

526 arm A was improved to decrease the numbers of photons entering the main body of the

527 reactor. Therefore, humidity correction is needed to accurately R_{meas}. The humidity

528 difference between C2 and C3 mode can be corrected by the function derived from the

529 relationship between OH reactivity and m37/m19 (as shown in Fig. 7 a).

530 **3.6 Instrument performance in ambient measurements**

531 The detection limit of ICRM was determined to be 2.3 s^{-1} for an averaged pyrrole-

532 to-OH ratio of 2.3 according to the method proposed by Michoud et al. (2015) (Fig S8).

533 This means that the minimum detection limit for the reactivity of sample air would be

534   about 5 s^{-1} (typically diluted in the glass reactor by a factor 2). During the measurement,

535   daily calibration was conducted by introducing a constant concentration of various

536   VOCs standards (propane, propene or toluene) through arm C at C2 mode and

537   determining the ratio of R_{meas} to R_{true} (i.e. α_{VOC}). As shown in Fig. S9, R_{meas} / R_{true} is

538   relatively stable during the measurement, ranging from 0.60 to 0.70, implying this

539   method has high stability, despite the structural differences of the VOCs species

540   introduced.

541   Figure 8 a presents a time series of R_{tot}, calculated OH reactivity (R_{cal}), and ambient

542   NO. R_{tot} was acquired based on Eq. 5, and R_{cal} is calculated by the sum of all measured

543   reactive trace gas concentrations multiplied by their respective reaction rate coefficients

544   with OH. The new system worked well even at high NO concentrations (> 20 ppbv).

545   The average R_{tot} for the entire campaign was 27.3 s^{-1}. The R_{tot} is higher than the R_{cal} by

546   27% during the campaign, with larger differences observed in the morning and at night

547   than in the afternoon. As shown in Fig. 8 b, the R_{tot} has an obvious diurnal variation

548   with higher levels at night and morning than that in the afternoon. This is because air

549   pollutants from anthropogenic emissions were accumulated at night and morning due

550   to lack of oxidative consumption, whereas were depleted rapidly during the afternoon

551   due to rising levels of oxidant, i.e. OH radicals. This diurnal pattern of R_{tot} is similar to

552   that of the previous measurement results in the Pearl River Delta (Lou et al., 2010; Yang

553   et al., 2017a) and Beijing (Williams et al., 2016). Overall, the diurnal variation of the

554    $R_{true\ VOC}$ (calculated by Eq.4) is similar to that of the calculated OH reactivity of

555   inorganic gas (Fig. 8 b) and the concentration of NO$_X$ (Fig. 8 c). A comparison between

556   the R_{tot} determined by the ICRM method and the laser-induced fluorescence method

557   will be of interest in future studies, particularly because LIF type systems can also

558   experience difficulties at high NO when OH decay rates are rapid. Further discussions

559   on the OH reactivity results of this campaign will be given in another publication.

4 Conclusion

561   In this study, we presented an improved comparative reactivity method (ICRM)

562   which is suitable for measuring OH reactivity under high-NO$_X$ conditions. The major

563 improvements of ICRM compared to the original CRM system are as follows:

564 (1) The HO_2 and RO_2 radicals produced from H radicals reacting with O_2 and OH-

565 oxidation of pyrrole, respectively, were removed continuously to the largest extent. In

566 this study, 50 ppbv NO was inject into the ICRM reactor through an additional arm G

567 between arm A and the reactor. Under this NO level, the interference due to the reaction

568 of HO_2 and RO_2 from pyrrole with NO was minimized.

569 (2) The OH recycling always happens to some extent when sampled VOCs are

570 introduced into the reactor in the presence of NO, causing the measured OH reactivity

571 (R_{meas}) deviate from the true OH reactivity (R_{true}). We quantified this effect by

572 calibrating several representative VOC species, CO and SO_2 to obtain the slope of R_{meas}

573 versus R_{true}. Different VOC species produce similar slopes, which are significantly

574 higher than the slopes of CO and SO_2. Using the average value of the derived slopes of

575 the different species as a correction factor, we obtained the more accurate R_{meas}.

576 Additionally, the effect of ambient NO on the difference between R_{true} and R'_{meas} was

577 quantified.

578 (3) Transforming the structure of the glass reactor to reduce the amount of ultraviolet

579 light generated by the mercury lamp reaching the main body of the glass reactor. This

580 effort resulted in eliminating the interference of pyrrole photolysis existed in the

581 original system. Under this condition, the new C1 mode used was able to avoid the

582 interference resulting from OH radicals produced by photolysis of residual humidity

583 and save lots of time compared with the original C1 mode. The ICRM system was

584 employed in a field campaign to measure OH reactivity and performed well even if

585 ambient NO concentrations are high.

586

587 **Data availability**

588   The more detailed data can be provided by contacting the corresponding author.

589

590 **Author contributions**

591   WJW and BY came up the idea for the improved CRM. JPQ built the ICRM system

and performed data analysis. WJW, JPQ and BY wrote the manuscript, with contributions from all other authors. YWP and SHW provided the PTR-TOF-MS and PAMS data. SXY helped the box model run. JW and VS revised the manuscript. MS provided the financial support.

Competing interests

The author declares that there is no conflict of interest.

Acknowledgment

This work was supported by Key-Area Research and Development Program of Guangdong Province (grant No. 2019B110206001), the National Natural Science Foundation of China (grant No. 41877302), Guangdong Natural Science Funds for Distinguished Young Scholar (grant No. 2018B030306037), the National Key R&D Plan of China (grant No. 2019YFE0106300, 2018YFC0213904, 2016YFC0202206), Guangdong Soft Science Research Program (2019B101001005), and Guangdong Innovative and Entrepreneurial Research Team Program (grant No. 2016ZT06N263). This work was also supported by Special Fund Project for Science and Technology Innovation Strategy of Guangdong Province (Grant No.2019B121205004).

References

A. Hofzumahaus, H. P. D., J. Callies, U. Platt and D. H. Ehhalt: Tropospheric OH concentration measurements by laser long-path absorption spectroscopy, Atmospheric Environment, 25A, 2017-2022, 1991.

Atkinson, R.: Atmospheric chemistry of VOCs and NOx, Atmospheric Environment, 36, 2063-2101, 2000.

Atkinson, R., Aschmann, S. M., Winer, A. M., and Carter, W. P. L.: Rate constants for the gas phase reactions of OH radicals and O_3, with pyrrole at 295 ± 1 K and atmospheric pressure, Atmospheric Environment, 18, 2105-2107, 1984.

Atkinson, R., Baulch, D. L., Cox, R. A., Crowley, J. N., Hampson, R. F., Hynes, R. G., Jenkin, M. E., Rossi, M. J., and Troe, J.: Evaluated kinetic and photochemical data for atmospheric chemistry: Volume I – gas phase reactions ofOx, HOx, NOx and SOx species, Atmospheric Chemistry and Physics, 4, 1461-1738, 2004.

Birks, J. W., Andersen, P. C., Williford, C. J., Turnipseed, A. A., Strunk, S. E., Ennis, C. A., and Mattson, E.: Folded tubular photometer for atmospheric measurements of NO_2 and NO, Atmospheric Measurement Techniques, 11, 2821-2835, doi: 10.5194/amt-11-2821-2018, 2018.

Cabanas, B., Baeza, M. T., Salgado, S., Martin, P., Taccone, R., and Martinez, E.: Oxidation of heterocycles in the atmosphere: Kinetic study of their reactions with NO3 radical, J. Phys. Chem. A, 108, 10818-10823, doi: 10.1021/jp046524t, 2004.

de Gouw, J. and Warneke, C.: Measurements of volatile organic compounds in the earth's atmosphere using proton-transfer-reaction mass spectrometry, Mass Spectrom Rev, 26, 223-257, doi: 10.1002/mas.20119, 2007.

Dillon, T. J., Tucceri, M. E., Dulitz, K., Horowitz, A., Vereecken, L., and Crowley, J. N.: Reaction of hydroxyl radicals with C_4H_5N (pyrrole): temperature and pressure dependent rate coefficients, J Phys Chem A, 116, 6051-6058, doi: 10.1021/jp211241x, 2012.

Dolgorouky, C., Gros, V., Sarda-Esteve, R., Sinha, V., Williams, J., Marchand, N., Sauvage, S., Poulain, L., Sciare, J., and Bonsang, B.: Total OH reactivity measurements in Paris during the 2010 MEGAPOLI winter campaign, Atmospheric Chemistry and Physics, 12, 9593-9612, doi: 10.5194/acp-12-9593-2012, 2012.

639   Fuchs, H., Novelli, A., Rolletter, M., Hofzumahaus, A., Pfannerstill, E. Y., Kessel, S., Edtbauer, A.,

640   Williams, J., Michoud, V., Dusanter, S., Locoge, N., Zannoni, N., Gros, V., Truong, F., Sarda-Esteve, R.,

641   Cryer, D. R., Brumby, C. A., Whalley, L. K., Stone, D., Seakins, P. W., Heard, D. E., Schoemaecker, C.,

642   Blocquet, M., Coudert, S., Batut, S., Fittschen, C., Thames, A. B., Brune, W. H., Ernest, C., Harder, H.,

643   Muller, J. B. A., Elste, T., Kubistin, D., Andres, S., Bohn, B., Hohaus, T., Holland, F., Li, X., Rohrer, F.,

644   Kiendler-Scharr, A., Tillmann, R., Wegener, R., Yu, Z. J., Zou, Q., and Wahner, A.: Comparison of OH

645   reactivity measurements in the atmospheric simulation chamber SAPHIR, Atmos. Meas. Tech., 10, 4023-

646   4053, doi: 10.5194/amt-10-4023-2017, 2017.

647   Hansen, R. F., Blocquet, M., Schoemaecker, C., Léonardis, T., Locoge, N., Fittschen, C., Hanoune, B.,

648   Stevens, P. S., Sinha, V., and Dusanter, S.: Intercomparison of the comparative reactivity method (CRM)

649   and pump–probe technique for measuring total OH reactivity in an urban environment, Atmospheric

650   Measurement Techniques, 8, 4243-4264, doi: 10.5194/amt-8-4243-2015, 2015.

651   Ingham, T., Goddard, A., Whalley, L. K., Furneaux, K. L., Edwards, P. M., Seal, C. P., Self, D. E., Johnson,

652   G. P., Read, K. A., Lee, J. D., and Heard, D. E.: A flow-tube based laser-induced fluorescence instrument

653   to measure OH reactivity in the troposphere, Atmospheric Chemistry and Physics, 2, 465-477, doi:

654   10.5194/amt-2-465-2009, 2009.

655   Kim, S., Guenther, A., Karl, T., and Greenberg, J.: Contributions of primary and secondary biogenic VOC

656   tototal OH reactivity during the CABINEX (Community Atmosphere-Biosphere INteractions

657   Experiments)-09 field campaign, Atmospheric Chemistry and Physics, 11, 8613-8623, doi: 10.5194/acp-

658   11-8613-2011, 2011.

659   Kim, S., Sanchez, D., Wang, M., Seco, R., Jeong, D., Hughes, S., Barletta, B., Blake, D. R., Jung, J.,

660   Kim, D., Lee, G., Lee, M., Ahn, J., Lee, S. D., Cho, G., Sung, M. Y., Lee, Y. H., Kim, D. B., Kim, Y.,

661   Woo, J. H., Jo, D., Park, R., Park, J. H., Hong, Y. D., and Hong, J. H.: OH reactivity in urban and suburban

662   regions in Seoul, South Korea - an East Asian megacity in a rapid transition, Faraday Discuss, 189, 231-

663   251, doi: 10.1039/c5fd00230c, 2016.

664   Kovacs, T. A. and Brune, W. H.: Total OH Loss Rate Measurement, Journal of Atmospheric Chemistry,

665   39, 105-122, doi: 10.1023/A:1010614113786, 2001.

666   Kovacs, T. A., Brune, W. H., Harder, H., Martinez, M., Simpas, J. B., Frost, G. J., Williams, E., Jobson,

667   T., Stroud, C., Young, V., Fried, A., and Wert, B.: Direct measurements of urban OH reactivity during

668   Nashville SOS in summer 1999, J Environ Monit, 5, 68-74, doi: 10.1039/b204339d, 2003.

669   Kumar, V., Chandra, B. P., and Sinha, V.: Large unexplained suite of chemically reactive compounds

670   present in ambient air due to biomass fires, Sci Rep, 8, 626, doi: 10.1038/s41598-017-19139-3, 2018.

671   Kumar, V. and Sinha, V.: VOC–OHM: A new technique for rapid measurements of ambient total OH

672   reactivity and volatile organic compounds using a single proton transfer reaction mass spectrometer,

673   International Journal of Mass Spectrometry, 374, 55-63, doi: 10.1016/j.ijms.2014.10.012, 2014.

674   Lou, S., Holland, F., Rohrer, F., Lu, K., Bohn, B., Brauers, T., Chang, C. C., Fuchs, H., Häseler, R., Kita,

675   K., Kondo, Y., Li, X., Shao, M., Zeng, L., Wahner, A., Zhang, Y., Wang, W., and Hofzumahaus, A.:

676   Atmospheric OH reactivities in the Pearl River Delta – China in summer 2006: measurement and model

677   results, Atmospheric Chemistry and Physics, 10, 11243-11260, doi: 10.5194/acp-10-11243-2010, 2010.

678   Michoud, V., Hansen, R. F., Locoge, N., Stevens, P. S., and Dusanter, S.: Detailed characterizations of

679   the new Mines Douai comparative reactivity method instrument via laboratory experiments and modeling,

680   Atmospheric Measurement Techniques, 8, 3537-3553, doi: 10.5194/amt-8-3537-2015, 2015.

681   Nölscher, A. C., Bourtsoukidis, E., Bonn, B., Kesselmeier, J., Lelieveld, J., and Williams, J.: Seasonal

682   measurements of total OH reactivity emission rates from Norway spruce in 2011, Biogeosciences, 10,

683   4241-4257, doi: 10.5194/bg-10-4241-2013, 2013.

684   Nölscher, A. C., Butler, T., Auld, J., Veres, P., Muñoz, A., Taraborrelli, D., Vereecken, L., Lelieveld, J.,

685   and Williams, J.: Using total OH reactivity to assess isoprene photooxidation via measurement and model,

686   Atmospheric Environment, 89, 453-463, doi: 10.1016/j.atmosenv.2014.02.024, 2014.

687   Nolscher, A. C., Sinha, V., Bockisch, S., Klupfel, T., and Williams, J.: Total OH reactivity measurements

688   using a new fast Gas Chromatographic Photo-Ionization Detector (GC-PID), Atmos. Meas. Tech., 5,

689   2981-2992, doi: 10.5194/amt-5-2981-2012, 2012a.

690   Nolscher, A. C., Williams, J., Sinha, V., Custer, T., Song, W., Johnson, A. M., Axinte, R., Bozem, H.,

691   Fischer, H., Pouvesle, N., Phillips, G., Crowley, J. N., Rantala, P., Rinne, J., Kulmala, M., Gonzales, D.,

692   Valverde-Canossa, J., Vogel, A., Hoffmann, T., Ouwersloot, H. G., de Arellano, J. V. G., and Lelieveld,

693   J.: Summertime total OH reactivity measurements from boreal forest during HUMPPA-COPEC 2010,

694   Atmospheric Chemistry and Physics, 12, 8257-8270, doi: 10.5194/acp-12-8257-2012, 2012b.

695   Pfannerstill, E. Y., Nölscher, A. C., Yáñez-Serrano, A. M., Bourtsoukidis, E., Keßel, S., Janssen, R. H.

696   H., Tsokankunku, A., Wolff, S., Sörgel, M., Sá, M. O., Araújo, A., Walter, D., Lavrič, J., Dias-Júnior, C.

697   Q., Kesselmeier, J., and Williams, J.: Total OH Reactivity Changes Over the Amazon Rainforest During

698   an El Niño Event, Frontiers in Forests and Global Change, 1, doi: 10.3389/ffgc.2018.00012, 2018.

699   Pfannerstill, E. Y., Reijrink, N. G., Edtbauer, A., Ringsdorf, A., Zannoni, N., Araújo, A., Ditas, F.,

700   Holanda, B. A., Sá, M. O., Tsokanku, A., Walter, D., Wolff, S., Lavrič, J. V., Pöhlker, C., Sörgel, M., and

701   Williams, J.: Total OH reactivity over the Amazon rainforest: variability with temperature, wind, rain,

702   altitude, time of day, season, and an overall budget closure, Atmospheric Chemistry and Physics

703   Discussions, doi: 10.5194/acp-2020-752, 2020. doi: 10.5194/acp-2020-752, 2020.

704   Pfannerstill, E. Y., Wang, N., Edtbauer, A., Bourtsoukidis, E., Crowley, J. N., Dienhart, D., Eger, P. G.,

705   Ernle, L., Fischer, H., Hottmann, B., Paris, J.-D., Stönner, C., Tadic, I., Walter, D., Lelieveld, J., and

706   Williams, J.: Shipborne measurements of total OH reactivity around the Arabian Peninsula and its role

707   in ozone chemistry, Atmospheric Chemistry and Physics, 19, 11501-11523, doi: 10.5194/acp-19-11501-

708   2019, 2019.

709   Praplan, A. P., Pfannerstill, E. Y., Williams, J., and Hellen, H.: OH reactivity of the urban air in Helsinki,

710   Finland, during winter, Atmos. Environ., 169, 150-161, doi: 10.1016/j.atmosenv.2017.09.013, 2017a.

711   Praplan, A. P., Pfannerstill, E. Y., Williams, J., and Hellén, H.: OH reactivity of the urban air in Helsinki,

712   Finland, during winter, Atmospheric Environment, 169, 150-161, doi: 10.1016/j.atmosenv.2017.09.013,

713   2017b.

714   Praplan, A. P., Tykkä, T., Chen, D., Boy, M., Taipale, D., Vakkari, V., Zhou, P., Petäjä, T., and Hellén, H.:

715   Long-term total OH reactivity measurements in a boreal forest, Atmospheric Chemistry and Physics, 19,

716   14431-14453, doi: 10.5194/acp-19-14431-2019, 2019a.

717   Praplan, A. P., Tykka, T., Chen, D., Boy, M., Taipale, D., Vakkari, V., Zhou, P. T., Petaja, T., and Hellen,

718   H.: Long-term total OH reactivity measurements in a boreal forest, Atmospheric Chemistry and Physics,

719   19, 14431-14453, doi: 10.5194/acp-19-14431-2019, 2019b.

720   Roger Atkinson, J. A.: Atmospheric Degradation of Volatile Organic Compounds, Chem. Rev., 103,

721   4605-4638, 2003.

722   Sadanaga, Y., Yoshino, A., Kato, S., and Kajii, Y.: Measurements of OH Reactivity and Photochemical

723   Ozone Production in the Urban Atmosphere, Environ. Sci. Technol. , 39, 8847-8852, doi:

724   10.1021/es049457p 2005.

725   Sadanaga, Y., Yoshino, A., Watanabe, K., Yoshioka, A., Wakazono, Y., Kanaya, Y., and Kajii, Y.:

726 Development of a measurement system of OH reactivity in the atmosphere by using a laser-induced

727 pump and probe technique, Review of Scientific Instruments, 75, 2648-2655, doi: 10.1063/1.1775311,

728 2004.

729 Sander, S. P., B. J. Finlayson-Pitts, R. R. Friedl, D. M. Golden, R. E. Huie, H. Keller-Rudek, C. E. Kolb,

730 M. J. Kurylo, M. J. Molina, G. K. Moortgat, V. L. Orkin, A. R. Ravishankara and P. H. Wine: Chemical

731 Kinetics and Photochemical Data for Use in Atmospheric Studies Evaluation Number 15, JPL

732 Publication 06-2, Jet Propulsion Laboratory, 2006.

733 Sinha, V., Custer, T. G., Kluepfel, T., and Williams, J.: The effect of relative humidity on the detection of

734 pyrrole by PTR-MS for OH reactivity measurements, International Journal of Mass Spectrometry, 282,

735 108-111, doi: 10.1016/j.ijms.2009.02.019, 2009.

736 Sinha, V., Williams, J., Crowley, J. N., and Lelieveld, J.: The Comparative Reactivity Method-a new tool

737 to measure total OH Reactivity in ambient air, Atmospheric Chemistry and Physics, 8, 2213-2227, doi:

738 10.5194/acp-8-2213-2008, 2008.

739 Sinha, V., Williams, J., Diesch, J. M., Drewnick, F., Martinez, M., Harder, H., Regelin, E., Kubistin, D.,

740 Bozem, H., Hosaynali-Beygi, Z., Fischer, H., Andrés-Hernández, M. D., Kartal, D., Adame, J. A., and

741 Lelieveld, J.: Constraints on instantaneous ozone production rates and regimes during DOMINO derived

742 using in-situ OH reactivity measurements, Atmospheric Chemistry and Physics, 12, 7269-7283, doi:

743 10.5194/acp-12-7269-2012, 2012.

744 Sinha, V., Williams, J., Lelieveld, J., Ruuskanen, T. M., Kajos, M. K., Patokoski, J., Hellen, H., Hakola,

745 H., Mogensen, D., Boy, M., Rinne, J., and Kulmala, M.: OH Reactivity Measurements within a Boreal

746 Forest: Evidence for Unknown Reactive Emissions, Environmental Science & Technology, 44, 6614-

747 6620, doi: 10.1021/es101780b, 2010.

748 Tan, Z. F., Lu, K. D., Hofzumahaus, A., Fuchs, H., Bohn, B., Holland, F., Liu, Y. H., Rohrer, F., Shao,

749 M., Sun, K., Wu, Y. S., Zeng, L. M., Zhang, Y. S., Zou, Q., Kiendler-Scharr, A., Wahner, A., and Zhang,

750 Y. H.: Experimental budgets of OH, HO2, and RO2 radicals and implications for ozone formation in the

751 Pearl River Delta in China 2014, Atmospheric Chemistry and Physics, 19, 7129-7150, doi: 10.5194/acp-

752 19-7129-2019, 2019.

753 Wang, M., Zeng, L., Lu, S., Shao, M., Liu, X., Yu, X., Chen, W., Yuan, B., Zhang, Q., Hu, M., and Zhang,

754 Z.: Development and validation of a cryogen-free automatic gas chromatograph system (GC-MS/FID)

for online measurements of volatile organic compounds, Anal. Methods, 6, 9424-9434, doi: 10.1039/c4ay01855a, 2014a.

Wang, Y., Ying, Q., Hu, J., and Zhang, H.: Spatial and temporal variations of six criteria air pollutants in 31 provincial capital cities in China during 2013-2014, Environ Int, 73, 413-422, doi: 10.1016/j.envint.2014.08.016, 2014b.

Williams, J., Keßel, S. U., Nölscher, A. C., Yang, Y., Lee, Y., Yáñez-Serrano, A. M., Wolff, S., Kesselmeier, J., Klüpfel, T., Lelieveld, J., and Shao, M.: Opposite OH reactivity and ozone cycles in the Amazon rainforest and megacity Beijing: Subversion of biospheric oxidant control by anthropogenic emissions, Atmospheric Environment, 125, 112-118, doi: 10.1016/j.atmosenv.2015.11.007, 2016.

Wolfe, G. M., Marvin, M. R., Roberts, S. J., Travis, K. R., and Liao, J.: The Framework for 0-D Atmospheric Modeling (F0AM) v3.1, Geoscientific Model Development, 9, 3309-3319, doi: 10.5194/gmd-9-3309-2016, 2016.

Wu, Y., Yang, Y. D., Shao, M., and Lu, S. H.: Missing in total OH reactivity of VOCs from gasoline evaporation, Chin. Chem. Lett., 26, 1246-1248, doi: 10.1016/j.cclet.2015.05.047, 2015.

Yang, Y., Shao, M., Keßel, S., Li, Y., Lu, K., Lu, S., Williams, J., Zhang, Y., Zeng, L., Nölscher, A. C., Wu, Y., Wang, X., and Zheng, J.: How the OH reactivity affects the ozone production efficiency: case studies in Beijing and Heshan, China, Atmospheric Chemistry and Physics, 17, 7127-7142, doi: 10.5194/acp-17-7127-2017, 2017a.

Yang, Y., Shao, M., Keßel, S., Li, Y., Lu, K., Lu, S., Williams, J., Zhang, Y., Zeng, L., Nölscher, A. C., Wu, Y., Wang, X., and Zheng, J.: How the OH reactivity affects the ozone production efficiency: case studies in Beijing and Heshan, China, Atmos. Chem. Phys., 17, 7127-7142, doi: 10.5194/acp-17-7127-2017, 2017b.

Yang, Y., Shao, M., Wang, X., Nölscher, A. C., Kessel, S., Guenther, A., and Williams, J.: Towards a quantitative understanding of total OH reactivity: A review, Atmospheric Environment, 134, 147-161, doi: 10.1016/j.atmosenv.2016.03.010, 2016.

Yuan, B., Koss, A. R., Warneke, C., Coggon, M., Sekimoto, K., and de Gouw, J. A.: Proton-Transfer-Reaction Mass Spectrometry: Applications in Atmospheric Sciences, Chem Rev, 117, 13187-13229, doi: 10.1021/acs.chemrev.7b00325, 2017.

Zannoni, N., Dusanter, S., Gros, V., Esteve, R. S., Michoud, V., Sinha, V., Locoge, N., and Bonsang, B.:

784   Intercomparison of two comparative reactivity method instruments inf the Mediterranean basin during

785   summer 2013, Atmos. Meas. Tech., 8, 3851-3865, doi: 10.5194/amt-8-3851-2015, 2015.

786   Zannoni, N., Gros, V., Lanza, M., Sarda, R., Bonsang, B., Kalogridis, C., Preunkert, S., Legrand, M.,

787   Jambert, C., Boissard, C., and Lathiere, J.: OH reactivity and concentrations of biogenic volatile organic

788   compounds in a Mediterranean forest of downy oak trees, Atmospheric Chemistry and Physics, 16, 1619-

789   1636, doi: 10.5194/acp-16-1619-2016, 2016.

790   Zannoni, N., Gros, V., Sarda Esteve, R., Kalogridis, C., Michoud, V., Dusanter, S., Sauvage, S., Locoge,

791   N., Colomb, A., and Bonsang, B.: Summertime OH reactivity from a receptor coastal site in the

792   Mediterranean Basin, Atmospheric Chemistry and Physics, 17, 12645-12658, doi: 10.5194/acp-17-

793   12645-2017, 2017.

794
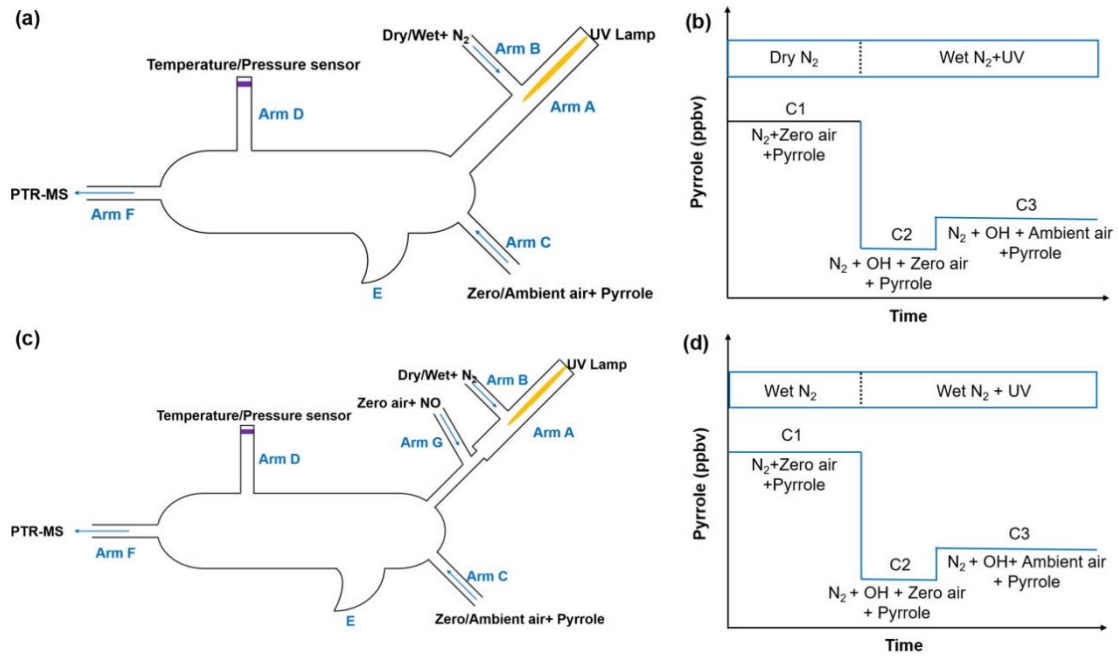
795

796 **Figure 1**. Schematic and work mode of the original CRM method (Sinha et al., 2008,

797 a and b) and the ICRM method (this study, c and d).
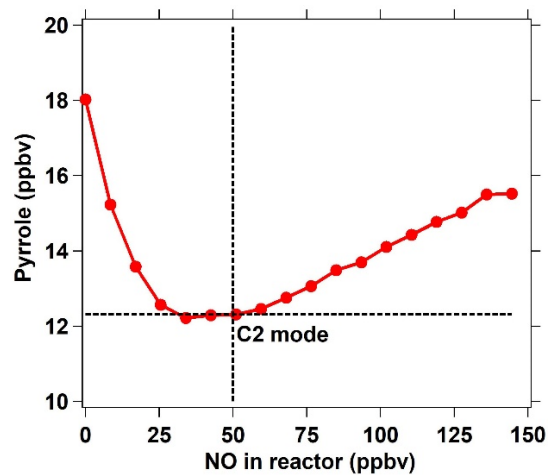
798

799 **Figure 2**. The response of pyrrole concentration to different NO concentrations
800 introduced through arm G into the reactor. For the ICRM system, the C2 mode is
801 corresponding to the pyrrole concentration = 12.31 ppbv at NO = 50 ppbv where the
802 HO_2 radicals were removed constantly.
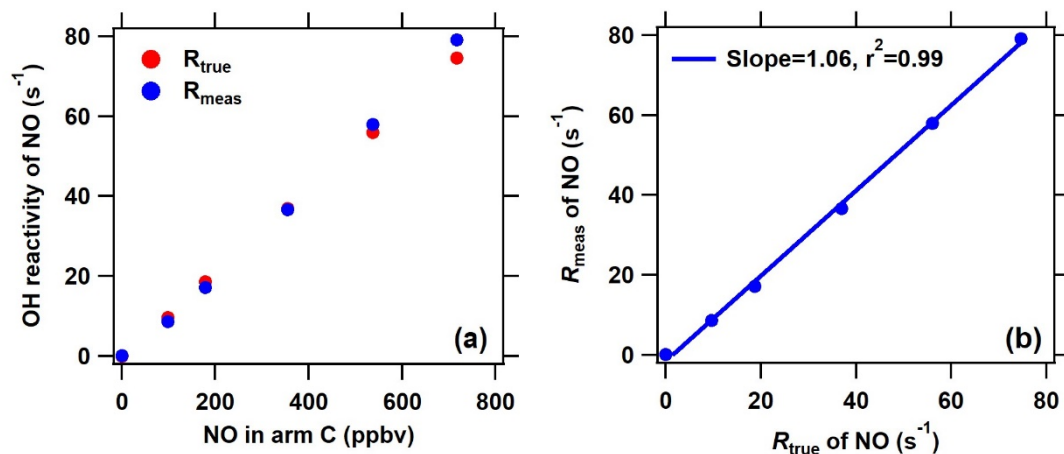
803

804 **Figure 3.** Comparison of measured and true OH reactivity of NO at different NO
805 concentrations introduced through arm C. The measured OH reactivity of NO was
806 calculated based on the new C2 mode shown in Fig. 2 in the ICRM system.

807
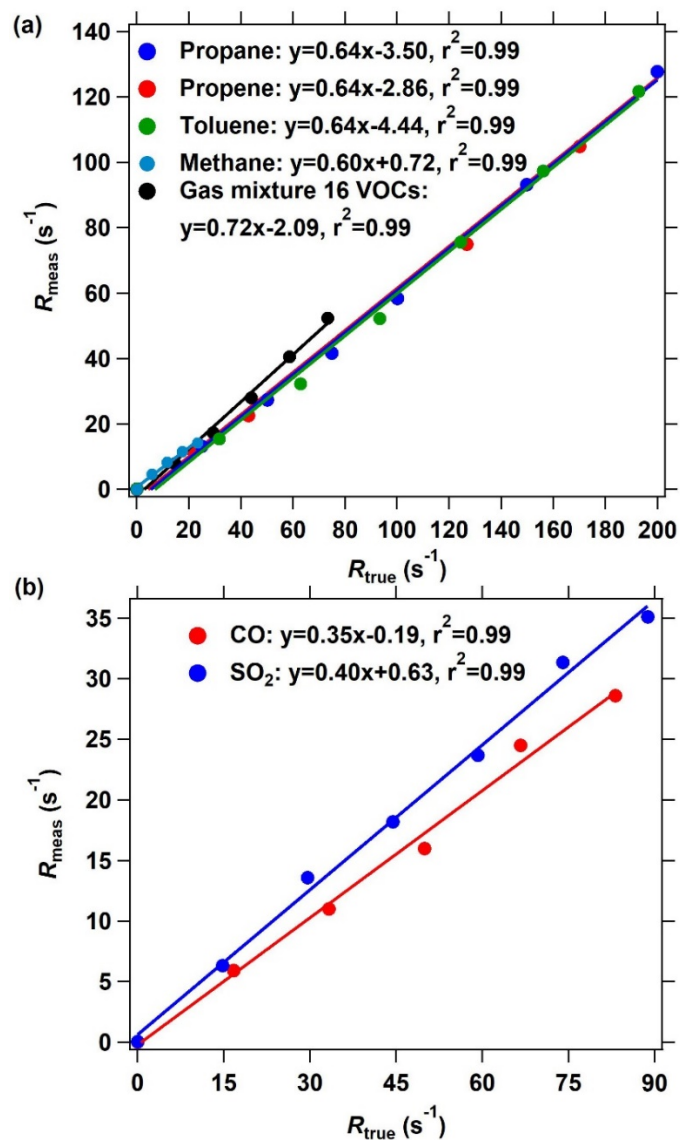
Figure 4. The OH reactivity calibration of the improved CRM system using different standard gases. **(a)** The calibrating results of organic species including methane, propane, propene, toluene, and a mixture of 16 VOC species through arm C. **(b)** The calibrating results of inorganic species including CO and SO_2. The measured OH reactivity was calculated based on the C2 mode shown in Fig. 2 in the ICRM system.

814
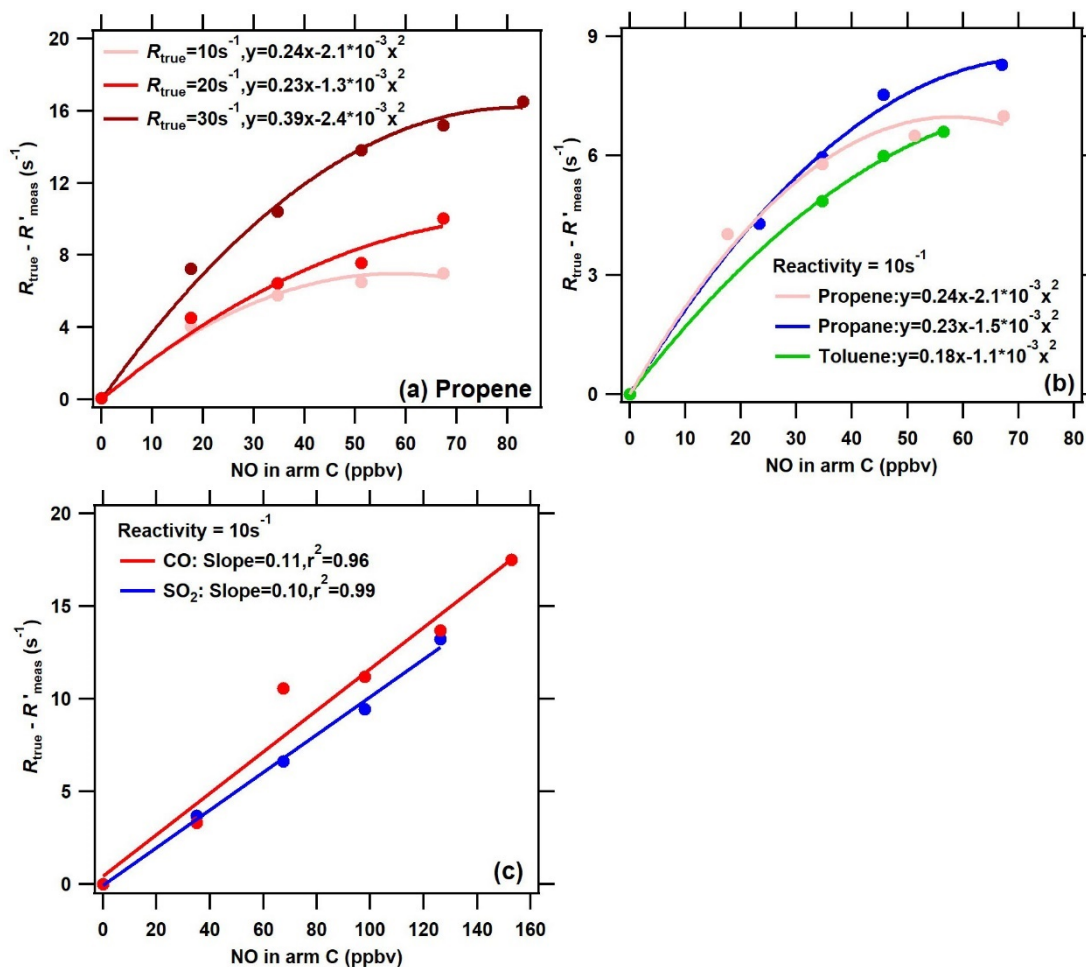
Figure 5. The difference between true OH reactivity (R_{true}) and the corrected measured OH reactivity (R'_{meas}) using the calibration factor α_1 ($R'_{meas} = (\frac{1}{\alpha_{VOC}} * R_{meas})$) as a function of NO concentrations in arm C in the conditions of **(a)** different levels of VOCs reactivity for the same species (propylene), **(b)** different VOCs species for the same OH reactivity level (10 s^{-1}), and **(c)** different inorganic species (Red: CO; Blue: SO$_2$) for the same OH reactivity level (10 s^{-1}). Note that NO, CO, SO$_2$, and VOCs were introduced into the reactor through arm C.
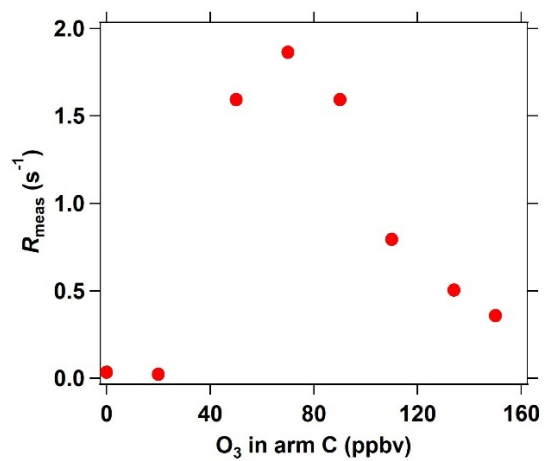
822

823 **Figure 6**. Interference of different O_3 concentration (introduced into the reactor through

824 arm C) on measured OH reactivity in the ICRM system.

825
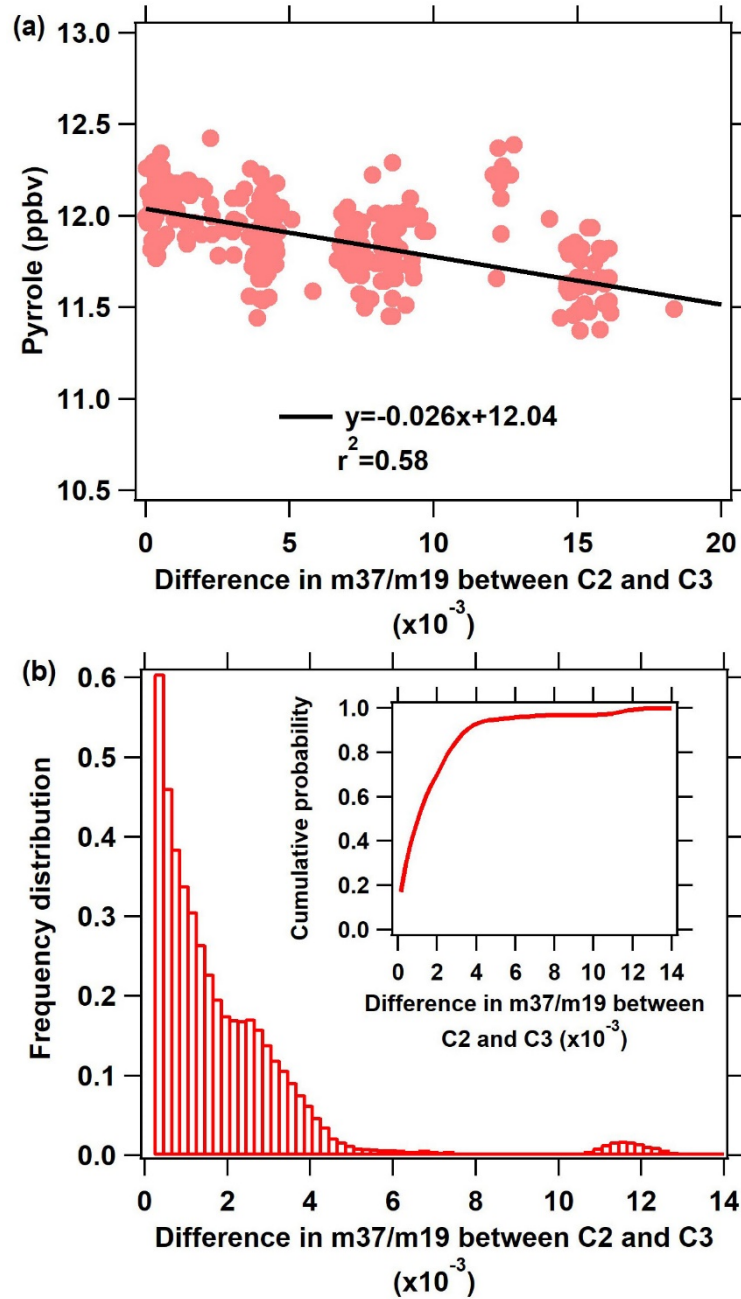
Figure 7. **(a)** Pyrrole concentration during zero air measurements (C2) as a function of the difference in m37/m19 between C2 and C3 humidity indicator (m37/m19). **(b)** Frequency distribution of the difference in m37/m19 between C2 and C3 during the measurement.

830

831
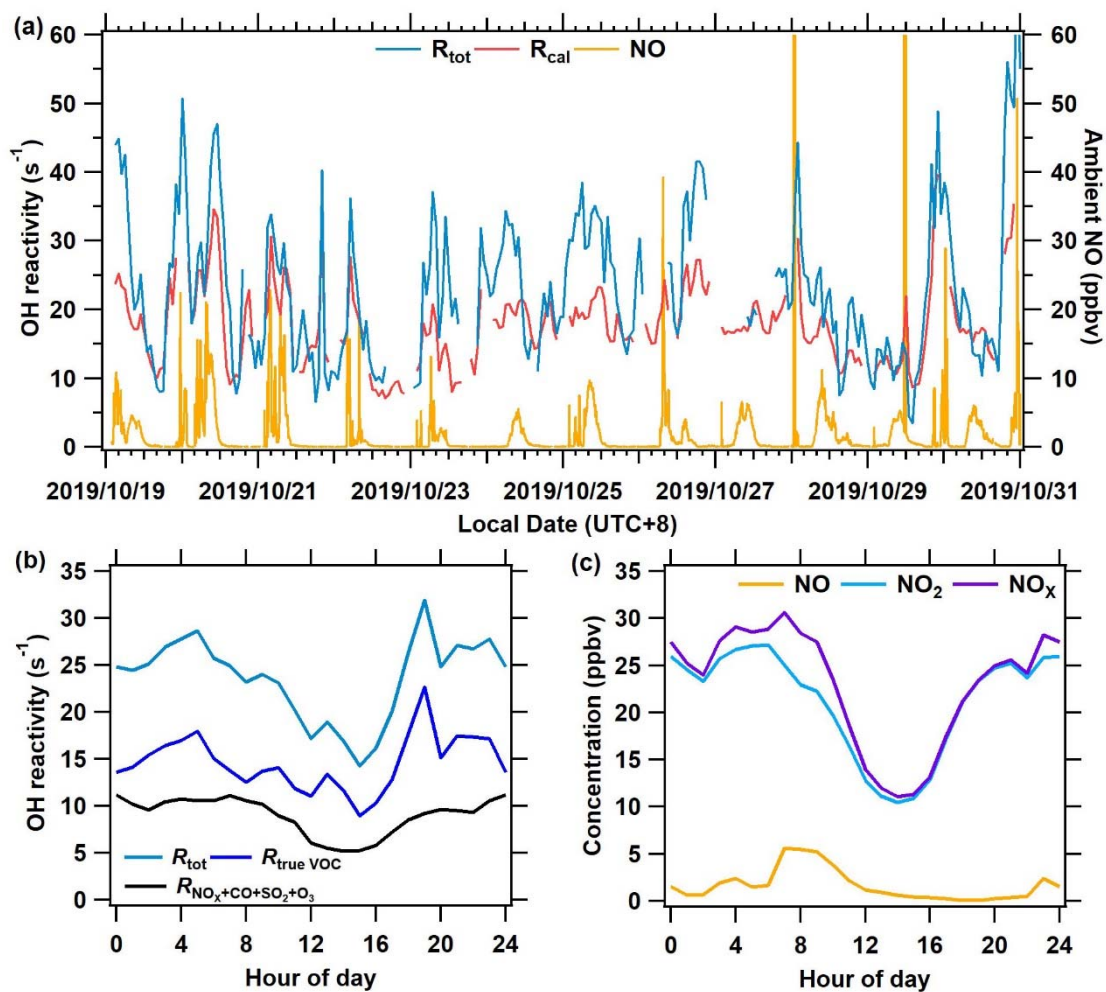
Figure 8. The measurement results of OH reactivity and ambient NO at the Heshan site from October 19 to October 31, 2019. **(a)** The time series of total OH reactivity (R_{tot}), calculated reactivity (R_{cal}), and ambient NO concentration; **(b)** Mean diurnal profile of OH reactivity of $R_{true\ VOC}$, $R_{NO_X+CO+SO_2+O_3}$, and R_{tot}; **(c)** Mean diurnal profiles of measured NO, NO_2, and NO_X.